THE JOURNAL OF PHYSICAL CHEMISTRY C
A JOURNAL OF THE AMERICAN CHEMICAL SOCIETY

pubs.acs.org/JPCC

Article

Silicon Cluster Arrays on the Monolayer of Hexagonal Boron Nitride on Ir(111)

Tobias Hartl, Daniel Herrmann, Moritz Will, Yannic Falke, Alexander Grüneis, Thomas Michely, and Pantelis Bampoulis*

Cite This: J. Phys. Chem. C 2022, 126, 6809−6814

Read Online

ACCESS | Metrics & More | Article Recommendations

ABSTRACT: Periodic structures of silicon are of interest in quantum-dot-based applications because of their unique optical and electronic properties. We report on the fabrication of stable quasi-ordered Si nanocluster arrays on the moiré of a hexagonal boron nitride (h-BN) monolayer on Ir(111). The h-BN monolayer promotes the growth of regular Si nanoclusters at 130 K and electronically decouples the clusters from the underlying metallic substrate. Using scanning tunneling microscopy and spectroscopy, we have investigated the cluster binding sites, their electronic structure, and their thermal stability. We find that the clusters display a size-dependent bandgap and that they are stable up to 577 K, after which cluster coalescence degrades the arrays.

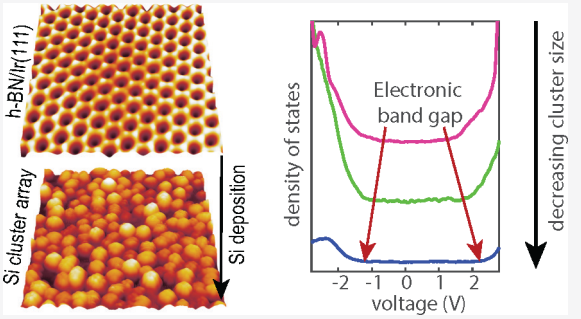

INTRODUCTION

Nanostructured materials exhibit novel and tunable properties that are much different from their bulk counterparts, and therefore hold great promise to advance current applications and inspire future ones.[1−3] Recent advancements in the formation of cluster superlattices with exceptional long-range order and controllable cluster sizes provide a roadmap to design bottom-up functional materials with the desired catalytic and electronic properties.[4−11] The fabrication of a silicon cluster superlattice is motivated by the clusters' potential in electronic and spintronic devices. For example, Si quantum dots have shown promise as active materials in qubit architectures for quantum computing[12−14] and display interesting charge transport characteristics.[15] Moreover, the photoluminescence and high quantum yield of Si nanoclusters make them also an interesting material for optoelectronic applications. The quantum size effect, resulting in a blue-shift of the energy gap, and surface passivation effects, limiting nonradiative recombination processes, are believed to be the heart of these optical properties.[16−22]

Despite the significance of Si to the current electronic industry, superlattices of small and stable Si nanoclusters have yet to be realized. Fabrication reproducibility and cluster disorder pose significant challenges, which could potentially limit the effectiveness and predictability of Si-cluster-based systems. The scalable fabrication of well-ordered arrays of Si nanoclusters integrated on an insulating substrate is anticipated to enable better utilization of their properties and encourage the use of Si clusters to advance the existing information technology. The use of similar-sized cluster arrays will allow easy patterning of electrical contacts anywhere on the array, making devices containing the desired cluster density.[23] Furthermore, the identical environment and similar size of the clusters will provide a collective response without smearing out the single cluster properties.

A monolayer of h-BN on Ir(111) system is an excellent template to grow arrays of similar-sized clusters. It provides (i) periodic nucleation sites where deposition of atoms lead to the growth of epitaxial and similar sized clusters,[24,25] (ii) the large bandgap of h-BN electronically decouples nanoclusters from the metallic Ir(111), preserving and allowing to measure their electronic structure.[25] We demonstrate that Si forms a quasi-ordered network of small clusters on h-BN when deposited at 130 K and have identified their binding sites. The Si nanoclusters display a wide range of sizes implying a large variety of the number of atoms between different clusters. Moreover, the nanoclusters are electronically decoupled from the underlying substrate and have a size-dependent energy bandgap.

EXPERIMENTAL METHODS

Sample preparation, STM, and LEED imaging were conducted in the ultrahigh-vacuum system ATHENE in Cologne. The

Received: January 28, 2022
Revised: March 25, 2022
Published: April 6, 2022

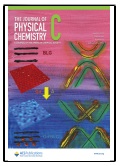

background base pressure was in the 10^{-11} mbar regime. Cleaning of the Ir(111) crystal was done by using several cycles of 2 keV Xe^+ sputtering and flash annealing to 1550 K. The h-BN monolayer was grown on Ir(111) by exposure to a background pressure of 5×10^{-9} mbar of borazine ($B_3N_3H_6$) at 1230 K. Borazine exposure was through a gas dosing tube which enhances the pressure at the sample location by a factor of 80. The h-BN monolayer was grown to near completion coverage as confirmed by STM and LEED experiments.

Si was evaporated on h-BN/Ir(111) and Ir(111) at 130 and 300 K from a home-built Si evaporator with a deposition rate of 0.11 MLE/min at an evaporation pressure around 1×10^{-9} mbar. The deposited amount θ was calibrated by Si deposition onto clean Ir(111) and subsequent annealing to 670 K for 30 min. The heating step leads to the formation of compact Si-induced islands. As we show in the main text, STM imaging was used for the determination of the island coverage and thus the deposition flux. The deposited amount of Si is given in monolayers with respect to the surface atomic density of Ir(111).

STM imaging was done at room temperature by using tunneling currents I in the range $I = 0.1-0.6$ nA and sample bias voltages U_s in the range $U_s = -(0.8-2.0)$ V. The STM data were processed (background subtraction and contrast adjustment) by using the WSxM software.[26]

RESULTS AND DISCUSSION

Figure 1a shows a large-scale scanning tunneling microscopy (STM) image of the Ir(111) surface after exposure to Si vapor at 300 K and annealing to 670 K for 30 min. The inset depicts structures (small clusters and wires) formed just after Si deposition at 300 K. After annealing, small Si-induced islands (marked with a black dashed outline) cover about 10% of the surface. The patches are grouped into two domains rotated by 13° with respect to each other as seen also in the fast Fourier transformation (FFT) of the topograph in Figure 1b. Figure 1c shows an atomically resolved image of a Si-induced island next to bare Ir(111). The island exhibits a complex reconstruction strongly resembling the $(\sqrt{19} \times \sqrt{19})$ $R23°$ reconstruction of the Si/Pt(111) system seen in STM and diffraction experiments.[27,28] Similar to Si/Pt(111), (i) the reconstructed Si/Ir(111) surface is located in the same atomic layer as the Ir(111)-(1 × 1), and the Ir(111)-(1 × 1) surface has the same level of apparent height with the basis of the Si-induced reconstruction; (ii) the reconstructed surface is modified by triangular-shaped features of dark and bright contrast rotated by about 23° with respect to the main directions of Ir(111); and (iii) it can be accurately described as a $(\sqrt{19} \times \sqrt{19})$ $R23°$ superstructure. The unit cell of the superstructure is indicated in Figure 1c, in which bright and dark triangular intrusions are in the unit cell. Therefore, the same atomistic model as for Si/Pt(111), in which the building block of the reconstruction is a Si_3Pt tetramer, can be adapted to Si/Ir(111). These observations rule out the growth of silicene on Ir(111) for submonolayer amounts of Si, in line with ref 29.

To limit Si−Ir alloying during cluster formation, we cover the Ir(111) crystal with a complete monolayer of h-BN. Figure 2a is a large-scale STM image of h-BN on Ir(111). The lattice mismatch between the two surfaces leads to the formation of a long-range moiré. The moiré periodicity amounts to 2.91 nm, a consequence of (11.7 × 11.7) h-BN unit cells matching (10.7 × 10.7) Ir unit cells.[30] Atomic-scale STM imaging (inset of

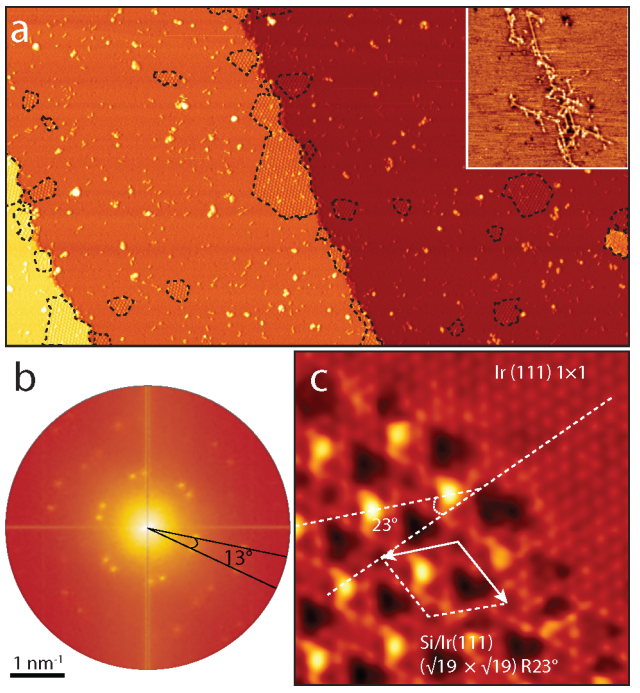

Figure 1. (a) Scanning tunneling microscopy (STM) topograph of Si-induced islands (marked with a black dashed outline) on Ir(111) after the deposition of Si at 300 K and annealing to 670 K for 30 min. Inset: Si-induced surface structures before the annealing step. (b) The corresponding FFT image revealing the two domains of the islands rotated by 13°. (c) An atomic scale STM image at the boundary of a Si-induced island and the Ir(111) pristine surface. The unit cell of the $(\sqrt{19} \times \sqrt{19})$ $R23°$ superstructure is overlaid on the image. The image sizes are 220 nm × 120 nm in (a), 33 nm × 33 nm in the inset of (a), and 5 nm × 5 nm in (c).

Figure 2a) reveals the h-BN atomic lattice—a honeycomb lattice with a period of 0.248 nm.[30] The corresponding FFT (Figure 2b) shows the first- and second-order moiré spots. Chemisorbed valleys appear as either dark depressions or bright protrusions with a darker interior depending on sample bias. They are separated by flat physisorbed mesas.[30] In the valleys, N atoms sit atop Ir atoms, leading to a partial sp^3 hybridization in h-BN and a higher reactivity at these sites.[30] Deposition of metals or C atoms on h-BN/Ir(111) results in the formation of regular arrays of clusters.[24,25] The clusters bind at the chemisorbed valleys modifying and strengthening the sp^3 binding motif.[25] Almost perfect superlattices of a variety of elements have been already created on h-BN/Ir(111).[24,25] These cluster superlattices display high thermal stability. For example, Ir and Pt cluster superlattices on h-BN/Ir(111) retain their order and number density up to 700 K,[24,25] more than 100 K higher temperatures than on h-BN/Rh(111)[31,32] and about 200 K higher than on Gr/Ir(111).[33] In addition, h-BN provides electronic decoupling of the clusters from the underlying metallic substrate.[25]

Deposition of 0.2 ML of Si on h-BN/Ir(111) at 300 K leads to the formation of small clusters and islands randomly scattered across the h-BN; compare Figure 2c and the corresponding FFT image in Figure 2d. This is in sharp contrast to the well-defined metal cluster superlattices,[24,25] indicating high mobility of the Si atoms on h-BN/Ir(111) at 300 K. To reduce the mobility of Si atoms, 0.2 ML of Si was deposited on h-BN at 130 K. At variance with the 300 K

https://doi.org/10.1021/acs.jpcc.2c00694
J. Phys. Chem. C 2022, 126, 6809−6814

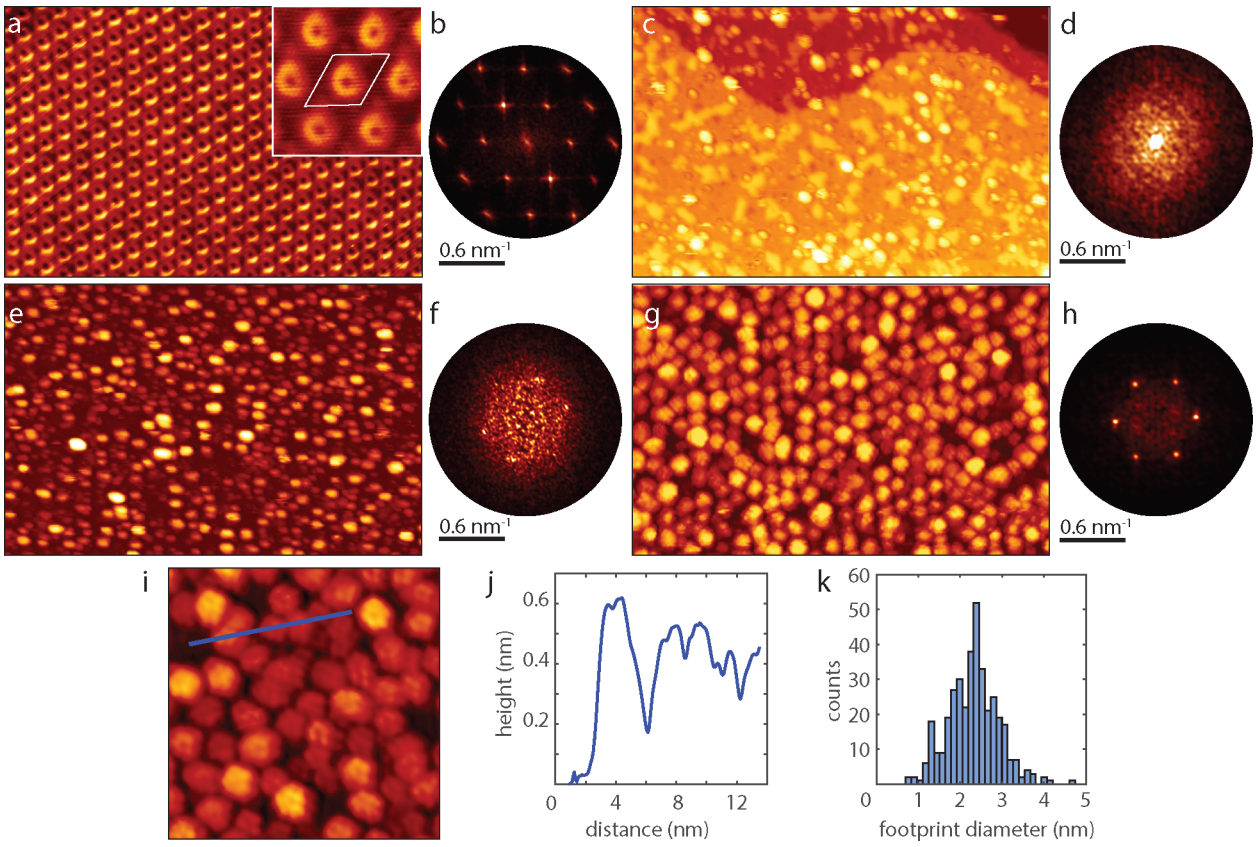

Figure 2. (a) Large-scale STM topograph of h-BN/Ir(111) showing the moiré superlattice. Inset: atomically resolved STM image of the h-BN/Ir(111) moiré superlattice with moiré unit cell indicated by the diamond of black lines. (b) The corresponding FFT image reveals the moiré spots. (c) The same sample after deposition of 0.2 ML of Si at 300 K; small Si clusters and islands are randomly scattered across the surface. This is also reflected by the diffuse FFT image in (d). (e) STM image of small Si clusters formed after deposition of 0.2 ML of Si on the clean h-BN/Ir(111) at 130 K. The Si nanoclusters display first signs of order reflected in the appearance of faint moiré spots in the FFT image in (f). (g) STM image of a Si cluster array formed after deposition of 0.4 ML of Si on the clean h-BN/Ir(111) at 130 K. The Si nanoclusters are quasi-ordered. (h) The corresponding FFT image shows the moiré spots. (i) Atomically resolved STM image of the Si nanoclusters on the h-BN/Ir(111) moiré. (j) Line profile across several clusters acquired along the blue line in (i). (k) A distribution of the footprint diameter of the clusters depicted in panel (g). The image sizes are 60 nm × 40 nm in (a), (c), (e), and (g), 13 nm × 13 nm in (i), and 7.5 nm × 7.5 nm in the inset of (a).

results, Si deposition at 130 K promotes self-organization of Si into small clusters covering the surface. The previously observed islands are absent (Figure 2e). Note that STM imaging is conducted at room temperature. The clusters show the first signs of order; weak but visible moiré spots can be discerned in the corresponding FFT image (Figure 2f).

Deposition of 0.4 ML of Si at 130 K improves cluster ordering and regularity. Figure 2g is an STM image recorded at room temperature of Si clusters formed after the deposition of 0.4 ML of Si on h-BN at 130 K. The corresponding FFT image (Figure 2h) shows well-defined hexagonal spots, indicating that many of the clusters follow the moiré periodicity of h-BN on Ir(111), forming an imperfect Si cluster superlattice. Several clusters are displaced from the superlattice points. There is also a small fraction of clusters occupying more than one lattice site.

High-resolution imaging of the clusters (Figure 2i) reveals a cluster structure resembling the molecular orbitals observed on C clusters,[34] fullerenes,[35,36] and sp^2-nanodiamonds.[37] This observation indicates that the Si clusters might be predominantly sp^2-hybridized. The observation is in line with the notion of endohedral Si fullerenes as a stable structural model for Si clusters consisting of a few tens of atoms.[38−40] In earlier theoretical studies the most stable cluster motif assumes a spherical compact structure, similar to the carbon fullerene cages. But in contrast to the empty C fullerenes, endohedral Si fullerenes consist of two shells of atoms. The outer shell is a fullerene-like sp^2-hybridized cage surrounding the inner shell, which is composed of stable atoms with saturated dangling bonds.[38] Figure 2j shows a line profile across several Si clusters (the location is indicated with the blue line in Figure 2i). The clusters have a height of about 0.5 nm, indicating a monolayer or a bilayer atom cage. Moreover, the clusters exhibit a wider range of lateral sizes (see the distribution of the footprint diameter in Figure 2k) compared to regular cluster superlattices,[24,25] implying a substantial variation of the number of Si atoms between different clusters. As is obvious from the STM and corresponding FFT images of Figure 2, the Si clusters have inferior order compared to the lattices formed by Pt, Ir, and C clusters on h-BN/Ir(111).[24,25]

To determine the preferred binding sites of Si clusters on h-BN, we intentionally removed several Si nanoclusters with the STM tip (Figure 3). This is achieved by scanning under low tunneling resistance conditions, suggesting a weak binding between Si and h-BN. The underlying h-BN moiré superlattice becomes again visible after cluster removal but appears to be defective. Nevertheless, the moiré lattice directions and the valley regions (darker regions) can be identified; these are the

https://doi.org/10.1021/acs.jpcc.2c00694
J. Phys. Chem. C 2022, 126, 6809−6814

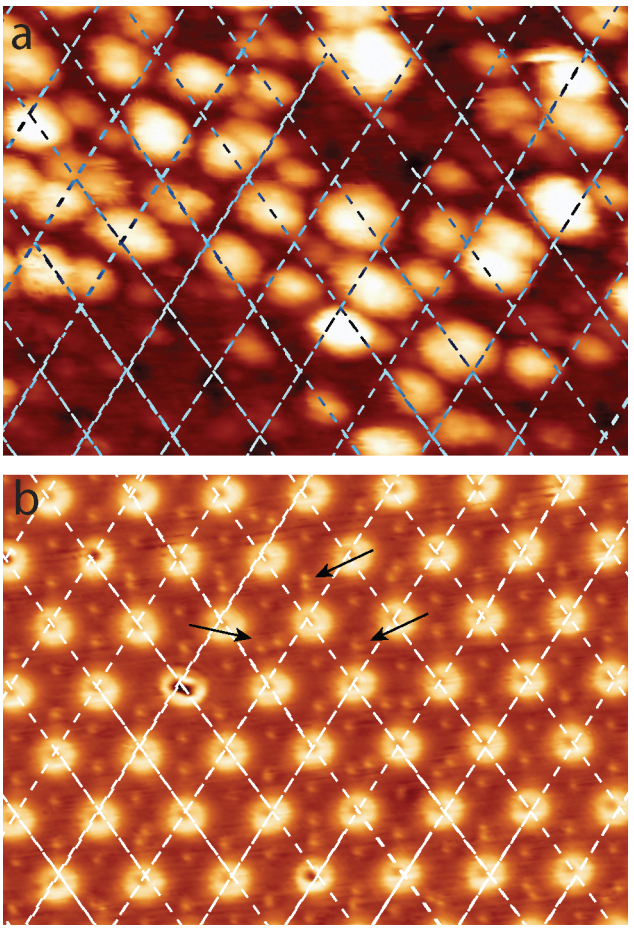

Figure 3. (a) STM topograph after deposition of 0.4 ML Si at 130 K and imaging at 300 K. In the lower half, the Si clusters have been removed with the STM tip. The grid of white dashed lines is matched to the center of the h-BN moiré valleys. (b) Atomically resolved STM image of the h-BN/Ir(111) moiré superlattice containing point defects (indicated with the black arrows) at the h-BN mesas. The image size is 20 nm × 15 nm in (a) and (b).

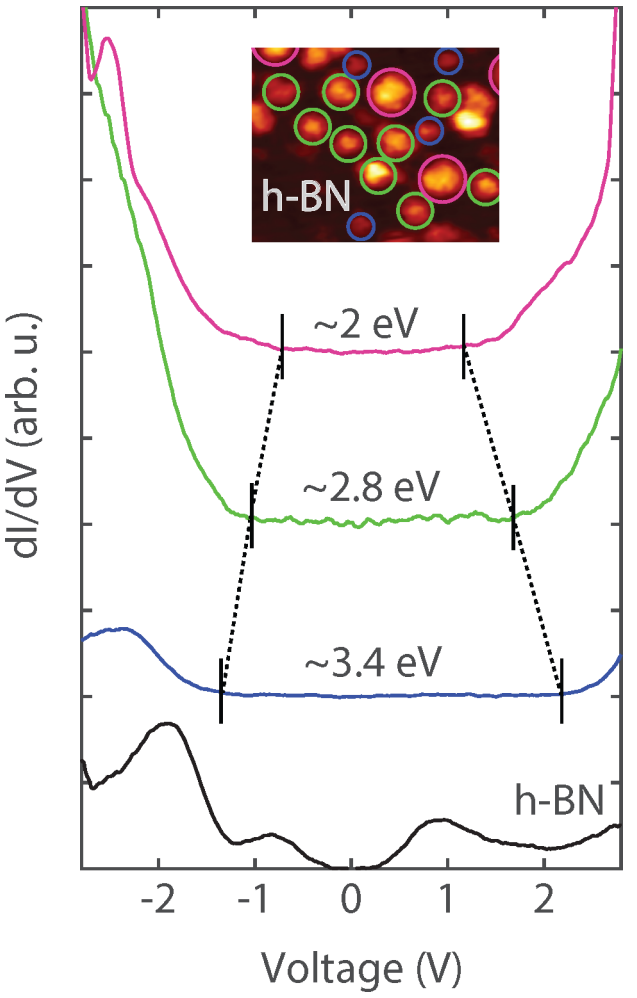

Figure 4. (a) Differential conductance dI/dV as a function of bias voltage V taken on h-BN/Ir(111) (black), small (blue), intermediate (green), and large (magenta) clusters, marked with the corresponding color in the topography inset (size: 13 nm × 16 nm). The spectra are the result of averaging over single spectra recorded at the center of Si clusters of similar size.

positions where the overlaid white dashed lines in Figure 3a cross each other. Surprisingly most of the clusters sit within mesa regions of the h-BN or are off-centered from the valleys. This observation suggests a preference toward the binding of Si to the mesa of h-BN. In comparison, clusters of Pt, Ir, and C bind at the more reactive valleys, i.e., regions where h-BN hybridizes with Ir.[24,25] At the mesa regions, it is common to find point defects already prior to deposition of Si, such as the ones visible in Figure 3b. The dangling bonds associated with such point defects and the orientation-specific Si bonds (contrary to metals) could be the cause of the stronger binding of Si at these locations. These competing binding sites lead to the imperfect order of the clusters.

Scanning tunneling spectroscopy was employed to study the electronic structure of Si nanoclusters on h-BN. Figure 4 shows numerically derived dI/dV (V) curves obtained on small (footprint diameter smaller than 1.5 nm), intermediate (footprint diameter of 2 ± 0.5 nm), and large Si clusters (footprint diameter larger than 2.5 nm) compared to the bare h-BN regions. Each curve is the result of averaging about 100 obtained on different but similarly sized clusters marked with blue for small clusters, green for intermediate clusters, and magenta for large clusters. While hBN exhibits no clear bandgap as a result of the hybridization of h-BN with Ir, the nanoclusters are clearly semiconductive. The h-BN template has sufficiently decoupled the nanoclusters from the underlying metal. Quantum confinement in the nanoclusters leads to an electronic bandgap that strongly depends on their size. Small clusters have a bandgap of about 3.4 eV, intermediate of 2.8 eV, and large of 2 eV. For the determination of the bandgaps, the curves were plotted in a logarithmic scale. The band edges were then estimated to be the points where the dI/dV signal starts to deviate with respect to the noise level. These bandgap values are significantly larger than the energy bandgap of bulk Si (1.1 eV) and are well within the theoretical calculations for small amorphous and crystalline Si clusters.[41]

Lastly, we have investigated the stability of the Si arrays upon annealing to high temperatures. Figure 5a shows a large-scale STM image of a Si nanocluster array formed at 130 K and imaged at 300 K. Figure 5b is the corresponding FFT image with the well-defined moiré spots. The quasi-ordered arrays of Si nanoclusters are stable up to 577 K. Annealing of the clusters to 577 K has no apparent influence on their size, shape, density, and order; see the topography in Figure 5c and the corresponding FFT in Figure 5d. Annealing to higher

https://doi.org/10.1021/acs.jpcc.2c00694
J. Phys. Chem. C 2022, 126, 6809−6814

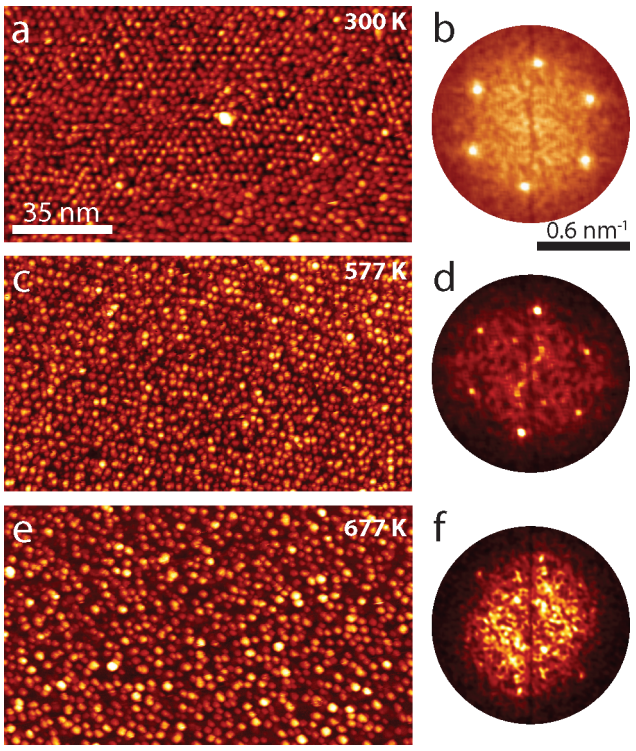

Figure 5. STM topographs and the corresponding FFT images of Si clusters formed on h-BN/Ir(111) by 0.4 ML Si deposition at 130 K. (a) The Si clusters were imaged at 300 K. (b) The corresponding FFT image of the STM image in (a). (c, d) STM image and the corresponding FFT after annealing to 577 K. (e, f) STM image and the corresponding FFT after annealing to 677 K. The image size in all panels is 130 nm × 75 nm.

temperatures leads to degradation of the arrays. Figures 5e and 5f show the STM and its FFT after the sample was annealed 677 K. The clusters arrays have lost their order, apparent from the weakened moiré spots and the increase of the diffuse background near the center of the FFT image. Many larger clusters are found across the surface, suggesting cluster array degradation through coalescence. Metal cluster arrays on h-BN/Ir(111) and Gr/Ir(111) degrade also through cluster coalescence albeit at higher annealing temperatures.[24,25,42]

CONCLUSIONS

The interaction of Si with the Ir(111) and the monolayer of h-BN on Ir(111) was investigated with scanning tunneling microscopy. Submonolayer amounts of Si form a surface alloy with the Ir(111) with a $(\sqrt{19} \times \sqrt{19})$ $R23°$ reconstruction. Deposition of Si on monolayer h-BN on Ir(111) at 130 K leads to the growth of an imperfect Si cluster superlattice. The nanocluster superlattice remains stable up to annealing temperatures of 677 K. The h-BN monolayer effectively decouples the nanoclusters from the underlying Ir(111) substrate, allowing to measure their size-dependent electronic bandgap. Small clusters have a bandgap of 3.4 eV, which decreases with increasing the size of the cluster, reaching a value of 2 eV for large Si clusters. We have identified the preferred Si binding site to be the mesa regions of h-BN, which is in contrast to the metal and C clusters formed similarly on h-BN. Point defects at the h-BN mesas possibly cause Si to bind at these locations.

AUTHOR INFORMATION

Corresponding Author

Pantelis Bampoulis − *II. Physikalisches Institut, Universität zu Köln, Cologne D-50937, Germany; Physics of Interfaces and Nanomaterials, MESA+ Institute for Nanotechnology, University of Twente, 7500 AE Enschede, The Netherlands;* orcid.org/0000-0002-2347-5223; Email: p.bampoulis@utwente.nl

Authors

Tobias Hartl − *II. Physikalisches Institut, Universität zu Köln, Cologne D-50937, Germany;* orcid.org/0000-0002-3881-5462

Daniel Herrmann − *II. Physikalisches Institut, Universität zu Köln, Cologne D-50937, Germany*

Moritz Will − *II. Physikalisches Institut, Universität zu Köln, Cologne D-50937, Germany;* orcid.org/0000-0003-4822-9122

Yannic Falke − *II. Physikalisches Institut, Universität zu Köln, Cologne D-50937, Germany*

Alexander Grüneis − *II. Physikalisches Institut, Universität zu Köln, Cologne D-50937, Germany;* orcid.org/0000-0003-2448-6060

Thomas Michely − *II. Physikalisches Institut, Universität zu Köln, Cologne D-50937, Germany*

Complete contact information is available at: https://pubs.acs.org/10.1021/acs.jpcc.2c00694

Notes

The authors declare no competing financial interest.

ACKNOWLEDGMENTS

This work was funded by the Deutsche Forschungsgemeinschaft (DFG, German Research Foundation) within the project "Cluster Superlattice Membranes" (project no. 452340798). P.B. gratefully acknowledges financial support from the Alexander von Humboldt Foundation.

REFERENCES

(1) Alivisatos, A. P. Semiconductor Clusters, Nanocrystals, and Quantum Dots. *Science* **1996**, *271*, 933−937.

(2) Heiz, U.; Landman, U. *Nanocatalysis*; Springer Science & Business Media: Heidelberg, 2007.

(3) Meiwes-Broer, K.-H. *Metal Clusters at Surfaces: Structure, Quantum Properties, Physical Chemistry*; Springer Science & Business Media: Heidelberg, 2000.

(4) N'Diaye, A. T.; Bleikamp, S.; Feibelman, P. J.; Michely, T. Two-Dimensional Ir Cluster Lattice on a Graphene Moiré on Ir(111). *Phys. Rev. Lett.* **2006**, *97*, 215501.

(5) Angelova, P.; Vieker, H.; Weber, N.-E.; Matei, D.; Reimer, O.; Meier, I.; Kurasch, S.; Biskupek, J.; Lorbach, D.; Wunderlich, e. A.; et al. Katrin A Universal Scheme to Convert Aromatic Molecular Monolayers into Functional Carbon Nanomembranes. *ACS Nano* **2013**, *7*, 6489−6497.

(6) Billinge, S. Materials Science: Nanoparticle Structures Served up on a Tray. *Nature* **2013**, *495*, 453−454.

(7) Henry, C. R. 2D-Arrays of Nanoparticles as Model Catalysts. *Catal. Lett.* **2015**, *145*, 731−749.

(8) Baltic, R.; Pivetta, M.; Donati, F.; Wäckerlin, C.; Singha, A.; Dreiser, J.; Rusponi, S.; Brune, H. Superlattice of Single Atom Magnets on Graphene. *Nano Lett.* **2016**, *16*, 7610−7615.

(9) Shi, Q.; Gómez, D. E.; Dong, D.; Sikdar, D.; Fu, R.; Liu, Y.; Zhao, Y.; Smilgies, D.-M.; Cheng, W. 2D Freestanding Janus Gold Nanocrystal Superlattices. *Adv. Mater.* **2019**, *31*, 1900989.

(10) Will, M.; Bampoulis, P.; Hartl, T.; Valerius, P.; Michely, T. Conformal Embedding of Cluster Superlattices with Carbon. *ACS Appl. Mater. Interfaces* **2019**, *11*, 40524−40532.
(11) Hartl, T.; Will, M.; Capeta, D.; Singh, R.; Scheinecker, D.; Boix de la Cruz, V.; Dellmann, S.; Lacovig, P.; Lizzit, S.; Senkovskiy, e. A.; Boris, V.; et al. Cluster Superlattice Membranes. *ACS Nano* **2020**, *14*, 13629−13637.
(12) Fuechsle, M.; Mahapatra, S.; Zwanenburg, F. A.; Friesen, M.; Eriksson, M. A.; Simmons, M. Y. Spectroscopy of Few-electron Single-crystal Silicon Quantum Dots. *Nat. Nanotechnol.* **2010**, *5*, 502−505.
(13) Stepina, N.; Zinov'eva, A.; Deryabin, A.; Zinov'ev, V.; Volodin, V.; Shklyaev, A.; Dvurechenskii, A.; Gaponenko, S. Formation and Structural Features of Silicon Quantum Dots in Germanium. *Optoelectron. Instrum. Data Process.* **2013**, *49*, 434−439.
(14) Cheng, J.-Y.; Fisher, B. L.; Guisinger, N. P.; Lilley, C. M. Atomically Manufactured Nickel−Silicon Quantum Dots Displaying Robust Resonant Tunneling and Negative Differential Resistance. *npj Quantum Mater.* **2017**, *2*, 1−6.
(15) Roland, C.; Meunier, V.; Larade, B.; Guo, H. Charge Transport Through Small Silicon Clusters. *Phys. Rev. B* **2002**, *66*, 035332.
(16) Cullis, A.; Canham, L. Visible Light Emission Due to Quantum Size Effects in Highly Porous Crystalline Silicon. *Nature* **1991**, *353*, 335−338.
(17) Trwoga, P.; Kenyon, A.; Pitt, C. Modeling the Contribution of Quantum Confinement to Luminescence from Silicon Nanoclusters. *J. Appl. Phys.* **1998**, *83*, 3789−3794.
(18) Dasog, M.; De los Reyes, G. B.; Titova, L. V.; Hegmann, F. A.; Veinot, J. G. Size vs Surface: Tuning the Photoluminescence of Freestanding Silicon Nanocrystals Across the Visible Spectrum via Surface Groups. *ACS Nano* **2014**, *8*, 9636−9648.
(19) Ledoux, G.; Guillois, O.; Porterat, D.; Reynaud, C.; Huisken, F.; Kohn, B.; Paillard, V. Photoluminescence Properties of Silicon Nanocrystals as a Function of their Size. *Phys. Rev. B* **2000**, *62*, 15942.
(20) Evlyukhin, A. B.; Reinhardt, C.; Seidel, A.; Luk'yanchuk, B. S.; Chichkov, B. N. Optical Response Features of Si-nanoparticle Arrays. *Phys. Rev. B* **2010**, *82*, 045404.
(21) Li, Q.; Jin, R. Photoluminescence from Colloidal Silicon Nanoparticles: Significant Effect of Surface. *Nanotechnol. Rev.* **2017**, *6*, 601−612.
(22) Park, N.-M.; Kim, T.-S.; Park, S.-J. Band Gap Engineering of Amorphous Silicon Quantum Dots for Light-Emitting Diodes. *Appl. Phys. Lett.* **2001**, *78*, 2575−2577.
(23) Whitham, K.; Yang, J.; Savitzky, B. H.; Kourkoutis, L. F.; Wise, F.; Hanrath, T. Charge Transport and Localization in Atomically Coherent Quantum Dot Solids. *Nat. Mater.* **2016**, *15*, 557−563.
(24) Will, M.; Atodiresei, N.; Caciuc, V.; Valerius, P.; Herbig, C.; Michely, T. A Monolayer of Hexagonal Boron Nitride on Ir(111) as a Template for Cluster Superlattices. *ACS Nano* **2018**, *12*, 6871−6880.
(25) Will, M.; Hartl, T.; Boix de la Cruz, V.; Lacovig, P.; Lizzit, S.; Knudsen, J.; Michely, T.; Bampoulis, P. Growth, Stability, and Electronic Decoupling of Pt Clusters on h-BN/Ir (111). *J. Phys. Chem. C* **2021**, *125*, 3880−3889.
(26) Horcas, I.; Fernández, R.; Gomez-Rodriguez, J.; Colchero, J.; Gómez-Herrero, J.; Baro, A. WSXM: A Software for Scanning Probe Microscopy and a Tool for Nanotechnology. *Rev. Sci. Instrum.* **2007**, *78*, 013705.
(27) Diebold, U.; Zhang, L.; Anderson, J. F.; Mrozek, P. Surface Segregation of Silicon in Platinum (111). *J. Vac. Sci. Technol.* **1996**, *14*, 1679−1683.
(28) Švec, M.; Hapala, P.; Ondráček, M.; Merino, P.; Blanco-Rey, M.; Mutombo, P.; Vondráček, M.; Polyak, Y.; Cháb, V.; Gago, e. A.; et al. JA Martin Silicene Versus Two-dimensional Ordered Silicide: Atomic and Electronic Structure of Si-(19× 19) R 23.4°/Pt (111). *Phys. Rev. B* **2014**, *89*, 201412.
(29) Satta, M.; Lacovig, P.; Apostol, N.; Dalmiglio, M.; Orlando, F.; Bignardi, L.; Bana, H.; Travaglia, E.; Baraldi, A.; Lizzit, S.; Larciprete, R. The Adsorption of Silicon on an Iridium Surface Ruling out Silicene Growth. *Nanoscale* **2018**, *10*, 7085−7094.
(30) Farwick zum Hagen, F. H.; Zimmermann, D. M.; Silva, C. C.; Schlueter, C.; Atodiresei, N.; Jolie, W.; Martinez-Galera, A. J.; Dombrowski, D.; Schroder, U. A.; et al. Moritz Structure and Growth of Hexagonal Boron Nitride on Ir (111). *ACS Nano* **2016**, *10*, 11012−11026.
(31) Martínez-Galera, A. J.; Gómez-Rodríguez, J. M. Pseudo-ordered Distribution of Ir Nanocrystals on h-BN. *Nanoscale* **2019**, *11*, 2317−2325.
(32) Düll, F.; Meusel, M.; Späth, F.; Schötz, S.; Bauer, U.; Bachmann, P.; Steinhauer, J.; Steinrück, H.-P.; Bayer, A.; Papp, C. Growth and Stability of Pt Nanoclusters from 1 to 50 atoms on h-BN/Rh (111). *Phys. Chem. Chem. Phys.* **2019**, *21*, 21287−21295.
(33) N'Diaye, A. T.; Gerber, T.; Busse, C.; Mysliveček, J.; Coraux, J.; Michely, T. A Versatile Fabrication Method for Cluster Superlattices. *New J. Phys.* **2009**, *11*, 103045.
(34) Herbig, C.; Knispel, T.; Simon, S.; Schröder, U. A.; Martínez-Galera, A. J.; Arman, M. A.; Teichert, C.; Knudsen, J.; Krasheninnikov, A. V.; Michely, T. From Permeation to Cluster Arrays: Graphene on Ir(111) Exposed to Carbon Vapor. *Nano Lett.* **2017**, *17*, 3105−3112.
(35) Lamb, L. D.; Huffman, D. R.; Workman, R. K.; Howells, S.; Chen, T.; Sarid, D.; Ziolo, R. F. Extraction and STM Imaging of Spherical Giant Fullerenes. *Science* **1992**, *255*, 1413−1416.
(36) Mararov, V. V.; Gruznev, D. V.; Bondarenko, L. V.; Tupchaya, A. Y.; Zotov, A. V.; Saranin, A. A. Comparative STM Analysis of C60 and C70 Fullerene Adsorption Sites on Pristine and Al-modified Si (111) 7× 7 Surfaces. *J. Vac. Sci. Technol.* **2016**, *34*, 061402.
(37) Pawlak, R.; Glatzel, T.; Pichot, V.; Schmidlin, L.; Kawai, S.; Fremy, S.; Spitzer, D.; Meyer, E. Local Detection of Nitrogen-Vacancy Centers in a Nanodiamond Monolayer. *Nano Lett.* **2013**, *13*, 5803−5807.
(38) Röthlisberger, U.; Andreoni, W.; Parrinello, M. Structure of Nanoscale Silicon Clusters. *Phys. Rev. Lett.* **1994**, *72*, 665.
(39) Ho, K.-M.; Shvartsburg, A. A.; Pan, B.; Lu, Z.-Y.; Wang, C.-Z.; Wacker, J. G.; Fye, J. L.; Jarrold, M. F. Structures of Medium-sized Silicon Clusters. *Nature* **1998**, *392*, 582−585.
(40) Yoo, S.; Shao, N.; Zeng, X. C. Structures and Relative Stability of Medium-and Large-sized Silicon Clusters. VI. Fullerene Cage Motifs for Low-lying Clusters Si_{39}, Si_{40}, Si_{50}, Si_{60}, Si_{70}, and Si_{80}. *J. Chem. Phys.* **2008**, *128*, 104316.
(41) Allan, G.; Delerue, C.; Lannoo, M. Electronic Structure of Amorphous Silicon Nanoclusters. *Phys. Rev. Lett.* **1997**, *78*, 3161.
(42) Gerber, T.; Knudsen, J.; Feibelman, P. J.; Granas, E.; Stratmann, P.; Schulte, K.; Andersen, J. N.; Michely, T. CO-Induced Smoluchowski Ripening of Pt Cluster Arrays on the Graphene/Ir(111) Moiré. *ACS Nano* **2013**, *7*, 2020−2031.

https://doi.org/10.1021/acs.jpcc.2c00694
J. Phys. Chem. C 2022, 126, 6809−6814